

Bad prospects for the detection of giant stars' tidal disruption: effect of the ambient medium on bound debris

Clément Bonnerot^{1*}, Elena M. Rossi¹ and Giuseppe Lodato²

¹*Leiden Observatory, Leiden University, PO Box 9513, 2300 RA, Leiden, the Netherlands*

²*Dipartimento di Fisica, Università Degli Studi di Milano, Via Celoria, 16, Milano, 20133, Italy*

Accepted ?. Received ?; in original form ?

ABSTRACT

Most massive galaxies are thought to contain a supermassive black holes in their centre surrounded by a tenuous gas environment, leading to no significant emission. In these quiescent galaxies, tidal disruption events represent a powerful detection method for the central black hole. Following the disruption, the stellar debris evolve into an elongated gas stream, which partly falls back towards the disruption site and accrete onto the black hole producing a luminous flare. Using an analytical treatment, we investigate the interaction between the debris stream and the gas environment of quiescent galaxies. Although we find dynamical effects to be negligible, we demonstrate that Kelvin–Helmholtz instability can lead to the dissolution of the stream into the ambient medium before it reaches the black hole, likely dimming the associated flare. Furthermore, we find this effect to be enhanced for disruptions involving more massive black holes and/or giant stars. Consequently, although disruptions of evolved stars have been proposed as a useful probe of black holes with masses $\gtrsim 10^8 M_\odot$, we argue that the associated flares are likely less luminous than expected.

Key words: black hole physics – hydrodynamics – galaxies: nuclei.

1 INTRODUCTION

Tidal disruption events (TDEs) occur when a star is scattered into a plunging orbit that brings it so close to a supermassive black hole (SMBH) that is torn apart by strong tidal forces (Frank & Rees 1976; Rees 1988). During the disruption, the stellar elements are forced into different trajectories, which causes the debris to subsequently evolve into an elongated gas stream. Half of the debris within this stream are bound to the black hole while the other half are unbound. After a revolution around the black hole, the bound ones return to the disruption site and form an accretion disc (Shiokawa et al. 2015; Hayasaki et al. 2013, 2015; Bonnerot et al. 2015), from which a powerful flare can be emitted (Komossa et al. 2004; Gezari et al. 2012, see Komossa 2015 for a recent review). This flare represents a unique probe to detect SMBHs in the centres of otherwise quiescent galaxies. Through this signal, it is also in principle possible to put constraints on the black hole properties as well as to investigate the physics of accretion and relativistic jets around these objects.

The debris evolution within the stream from disruption to their return to pericentre has been the focus of several studies, both numerical and analytical. While the debris fol-

low close to ballistic orbits, the transverse structure of the stream is set by the equilibrium between the different forces acting in this direction. During most of its evolution, internal pressure is balanced by self-gravity, which causes the stream to maintain a narrow profile (Kochanek 1994; Ramirez-Ruiz & Rosswog 2009; Guillochon et al. 2014). However, a recent simulation shows that internal pressure inside the stream may be unable to prevent the fragmentation of the debris into self-gravitating clumps, which can form a few years after disruption (Coughlin & Nixon 2015; Coughlin et al. 2015).

Although it is not associated to substantial emission, a gas component is present around SMBHs in the centre of quiescent galaxies. It is commonly assumed to originate from stellar winds released by massive stars surrounding the black hole (Quataert 2004; Cuadra et al. 2006; Generozov et al. 2015). The impact of this gaseous environment on the stream evolution has so far been largely ignored, owing to a large density contrast between the two components. In a recent study, Guillochon et al. (2015) find that it can affect the trajectories of the unbound debris, resulting in their deceleration on parsec scales. Other authors looked into the influence on the bound part of the stream but in specific contexts, such as a possible origin for the G2 cloud (Guillochon et al. 2014) and the interaction with a fossil accretion disc (Kelley et al. 2014).

In this paper, we investigate the influence of the ambient

* E-mail: bonnerot@strw.leidenuniv.nl

gas on the bound debris in a general way. Although dynamical effects on these debris are negligible, we demonstrate that hydrodynamical instabilities can lead to the dissolution of a significant part of these debris into the gaseous environment before they return to pericentre. In this situation, we argue that the associated TDE would be significantly dimmer than expected. This effect is enhanced when the disruption involves a giant star and/or a more massive black hole. As a result, TDEs involving black holes of mass $\gtrsim 10^8 M_\odot$ could be difficult to detect. While main sequence stars are swallowed whole by such black holes leading to no substantial emission (MacLeod et al. 2012), disruptions of giant stars could be just as dim owing to the dissolution of the debris into the ambient medium.

This paper is organized as follows. Sections 2 and 3 present the models used for the SMBH gaseous environment and the debris stream respectively. Section 4 investigates the interaction between these two components through both ram pressure and hydrodynamical instabilities. In Section 5, we determine the impact on the detectability of TDEs. Our concluding remarks are found in Section 6.

2 GASEOUS ENVIRONMENT MODEL

In quiescent galaxies, black holes are surrounded by accretion flows, whose gas is mostly supplied by stellar winds from massive stars. The density distribution within this flow is given by the interplay between their hydrodynamics and the efficiency of the supply mechanism.

The Milky Way is the best example of a quiescent galaxy. It harbours Sgr A*, a central black hole of mass $4.3 \times 10^6 M_\odot$, surrounded by a gas environment well studied both theoretically and observationally. Analytical models of stellar winds sources find a density profile in the inner region of the flow decreasing as R^{-1} (Quataert 2004; Genozov et al. 2015), a result consistent with numerical simulations (Cuadra et al. 2006).

Based on this example, we adopt a simple gas density profile for the inner region of quiescent galaxies, given by¹

$$\rho_g(R) = \rho_0 \left(\frac{R}{R_0} \right)^{-1}, \quad (1)$$

For the Milky Way, the normalization is inferred from Chandra X-ray observations at the Bondi radius, which find a density $\rho_{0,\text{MW}} = 2.2 \times 10^{-22} \text{ g cm}^{-3}$ at $R_{0,\text{MW}} = 0.04 \text{ pc}$.

For galaxies hosting SMBHs of different masses, this profile is scaled using the black hole radius of influence

$$R_{\text{inf}} = \frac{GM_{\text{h}}}{\sigma^2} \simeq 3 \text{ pc} \left(\frac{M_{\text{h}}}{4.3 \times 10^6 M_\odot} \right)^{7/15}, \quad (2)$$

where M_{h} is the black hole mass, σ is the velocity dispersion of stars in the bulge and the second equality uses the $M_{\text{h}} -$

¹ In our galaxy, a density profile scaling as $R^{-1/2}$ may be more consistent with observations of the inner accretion flow (Wang et al. 2013). In other quiescent galaxies, this slope can be derived from observations of TDEs featuring outflows, where it is found to be steeper, decreasing as $R^{-5/2}$ (Alexander et al. 2015) or $R^{-3/2}$ (Berger et al. 2012). However, this could be caused by the propagation of the outflow into a previously evacuated funnel.

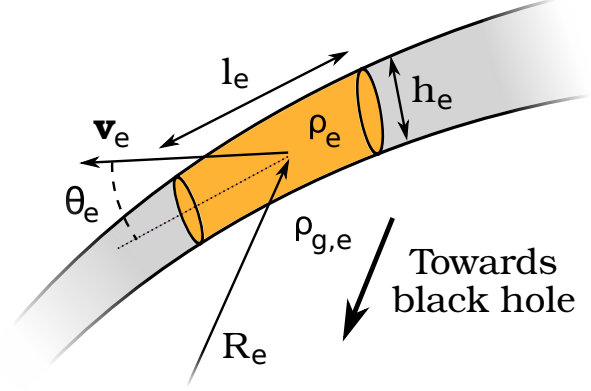


Figure 1. Sketch of a portion of debris stream with an element shown in orange. The element has a cylindrical geometry, with length l_e and width h_e . Its density ρ_e is obtained from equation (5) knowing its mass. At a distance R_e from the black hole, it moves through a gaseous environment of density $\rho_{g,e} \equiv \rho_g(R_e)$ with a velocity \mathbf{v}_e , inclined with respect to its longitudinal axis by an angle θ_e .

σ relation $M_{\text{h}} = 2 \times 10^8 (\sigma/200 \text{ km s}^{-1})^{15/4} M_\odot$ (Gebhardt et al. 2000)². The normalization radius is then obtained from

$$R_0 = \left(\frac{M_{\text{h}}}{4.3 \times 10^6 M_\odot} \right)^{7/15} R_{0,\text{MW}}. \quad (3)$$

The normalization density is computed by assuming spherical accretion at a velocity $v \propto v_{\text{ff}} \propto M_{\text{h}}^{1/2} R^{-1/2}$, where v_{ff} is the free-fall velocity. It leads to an accretion rate $\dot{M} \propto R_0^2 \rho_0 v(R_0) \propto \rho_0 M_{\text{h}}^{6/5}$ using equation (3). The gas is supplied to the accretion flow by stellar winds from stars within the black hole sphere of influence. As the mass of stars is similar to that of the black hole within this distance, $\dot{M} \propto M_{\text{h}}$. This yields

$$\rho_0 = \eta \left(\frac{M_{\text{h}}}{4.3 \times 10^6 M_\odot} \right)^{-1/5} \rho_{0,\text{MW}}, \quad (4)$$

where η is a parameter, equal to 1 for the Milky Way. In the following, it is varied up to 10^3 to investigate galaxies with denser gas environments. This simple scaling of the gas density profile has also been used by Rimoldi et al. (2015). It leads to a similar dependence on M_{h} as found from a more detailed treatment (Genozov et al. 2015).

3 TIDAL STREAM MODEL

The disruption of a star of mass M_* and radius R_* occurs when it reaches the tidal radius $R_t = R_*(M_{\text{h}}/M_*)^{1/3}$. The resulting debris evolve into an elongated stream owing to an orbital energy spread $\Delta\epsilon = GM_{\text{h}}R_*/R_t^2$, acquired during the disruption. In this work, we only focus on the bound debris, with orbital energies ϵ from $-\Delta\epsilon$ to 0 and periods T between $t_{\text{min}} = 2\pi GM_{\text{h}}(2\Delta\epsilon)^{-3/2}$ and $+\infty$.

To model the stream of bound debris, we divide it into

² The $M_{\text{h}} - \sigma$ relation can be steeper than this. However, our results are essentially unchanged when using a steeper $M_{\text{h}} \propto \sigma^{5.3}$ relation (McConnell et al. 2011).

cylindrical elements, an example of which is sketched in Fig. 1. In the following, the variables associated to a particular element are indicated by the subscript “e” to differentiate them from those associated to the debris.

An element of period T_e contains debris whose periods satisfy $T_e - \delta T_e < T < T_e + \delta T_e$. Equivalently, it has an average orbital energy $\epsilon_e = -(1/2)(2\pi GM_h/T_e)^{2/3}$ and contains debris with orbital energies in the range $\epsilon_e - \delta\epsilon_e < \epsilon < \epsilon_e + \delta\epsilon_e$. To ensure that each element is composed of debris with similar periods, we set $\delta T_e = 10^{-2} t_{\min} \ll T_e$.

Following the disruption, each component of the stream is assumed to follow Keplerian orbits with the same pericentre R_t but different orbital energies ϵ . The position \mathbf{x}_e and velocity \mathbf{v}_e of an element are identified with those of the debris with orbital energy ϵ_e .

Owing to its cylindrical geometry, the density of an element is obtained by

$$\rho_e = \frac{m_e}{\pi h_e^2 l_e}, \quad (5)$$

where m_e , h_e and l_e denote the mass, width and length of the element respectively. We explain how these quantities are computed in the remaining of this section.

Knowing the separation $\delta\mathbf{x}_e$ of its two extremities, the length of an element is obtained by $l_e = |\delta\mathbf{x}_e|$. Its velocity \mathbf{v}_e is inclined with respect to its longitudinal direction by an angle θ_e obtained by $\cos\theta_e = \mathbf{v}_e \cdot \delta\mathbf{x}_e / (|\mathbf{v}_e| |\delta\mathbf{x}_e|)$.

The mass m_e of an element is obtained from

$$m_e = \int_{\epsilon_e - \delta\epsilon_e}^{\epsilon_e + \delta\epsilon_e} dM \simeq 2 \left. \frac{dM}{d\epsilon} \right|_{\epsilon_e} \delta\epsilon_e. \quad (6)$$

where $dM/d\epsilon$ is the debris orbital energy distribution. The latter is computed using the analytical model developed by Lodato et al. (2009), which assumes that the energy of the debris is given by their depths within the black hole potential when the star is disrupted. This yields

$$\frac{dM}{d\epsilon} = \frac{R_\star}{\Delta\epsilon} \int_{\Delta r}^{R_\star} 2\pi\rho_\star(r)r dr, \quad (7)$$

where ρ_\star is the density inside the star and $\Delta r = (\epsilon/\Delta\epsilon)R_\star$. This allows to compute the fallback rate of the debris to pericentre, given by

$$\dot{M}_{\text{fb}} = \frac{dM}{d\epsilon} \frac{d\epsilon}{dT} = \frac{(2\pi GM_h)^{2/3}}{3} \frac{dM}{d\epsilon} T^{-5/3}, \quad (8)$$

where the relation $T = 2\pi GM_h(-2\epsilon)^{-3/2}$ is used in the second equality.

Based on the work by MacLeod et al. (2012), different density profiles are considered corresponding to the evolution of a $1.4 M_\odot$ star. They are obtained from a detailed simulation of the star using the stellar evolution code MESA (Paxton et al. 2011). The evolution of the stellar radius is shown in Fig. 2, with the main phases of evolution indicated by filled areas and the five stellar density profiles considered later in the paper shown with coloured points. In the main sequence phase (green area), one profile is considered (MS). Two profiles are chosen in the red giant phase (yellow area): when the star is ascending the red giant branch (RG1) and when it reached the tip of this branch (RG2). For the horizontal branch (orange area) and the asymptotic giant branch (red area) phases, two profiles are selected (HB and AGB).

The width h_e is obtained by assuming hydrostatic equi-

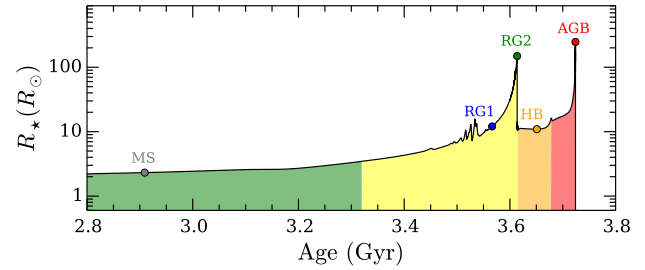


Figure 2. Evolution of the radius of a $1.4 M_\odot$ star. The main evolutionary phases are indicated by filled regions: main sequence (green), red giant (yellow), horizontal branch (orange) and asymptotic giant branch (red). The coloured points correspond to the five stellar density profiles considered.

librium in the stream transverse direction. While pressure tends to expand the stream, the tidal force from the black hole and the stream self-gravity oppose this expansion. Note that the tidal force acts inwards since the stream transverse direction is close to that orthogonal to the direction of the black hole. Hydrostatic equilibrium thus reduces to

$$a_{p,e} = a_{t,e} + a_{g,e} \quad (9)$$

where $a_{p,e} = \nabla P_e / \rho_e \simeq P_e / (\rho_e h_e)$ is the pressure acceleration, $a_{t,e} \simeq GM_h h_e / R_e^3$ is the tidal acceleration and $a_{g,e} \simeq Gm_e / (h_e l_e)$ is the self-gravity acceleration within the stream, $R_e = |\mathbf{x}_e|$ being the distance from the black hole and P_e the pressure in the stream. For the pressure, we assume an adiabatic evolution with $P_e = K\rho_e^\gamma$ where $\gamma = 5/3$. Although the adiabatic constant K should a priori be different for different elements, we adopt a single value averaged over the volume of the star. This is legitimate as the value of K within the star varies only by a factor of a few around this average. The width h_e is obtained by solving equation (9), making use of equation (5). For illustration, in the two limiting cases $a_{g,e} \gg a_{t,e}$ and $a_{g,e} \ll a_{t,e}$, it scales as $h_e \propto (m_e/l_e)^{-1/4}$ and $h_e \propto (R_e^3/M_h)^{3/10} (m_e/l_e)^{-1/5}$ respectively.

4 TIDAL STREAM - AMBIENT MEDIUM INTERACTIONS

4.1 Hydrodynamical instabilities

As the stream moves through the ambient medium, it is subject to Kelvin–Helmholtz (K-H) instability. In this section, we evaluate the effect of this instability on each stream element.

Taking a conservative approach, we only consider the second half of each element orbit, i.e. after apocentre passage. This approach is motivated by the fact that an element reaches its lowest density in this part of the orbit and is therefore more easily affected by its interaction with the ambient medium. In this portion of the orbit, an element falls almost radially from apocentre to pericentre. In this configuration, K-H instability develops on a given stream element for wavenumbers k_e which obey the inequality (Clarke & Carswell 2007, p.138)

$$a_e < \frac{\rho_e \rho_{g,e}}{\rho_e^2 - \rho_{g,e}^2} k_e^2 v_{\text{rel},e}^2 \quad (10)$$

where a_e is the inwards acceleration of the element in the transverse direction, $\rho_{g,e} \equiv \rho_g(R_e)$ is the density of gas at the position of the element and $v_{rel,e}$ is the relative velocity between the element and the background gas. Although modes with large k_e have fast growth rates, they are also the least disruptive as the associated instability saturates at an amplitude $\sim 1/k_e$. We therefore consider a wavenumber $k_e = 1/h_e$ which has the slowest growth rate but is the most disruptive since it develops on the whole element width. The transverse acceleration a_e has two inwards components. One is the self-gravity acceleration $a_{g,e} \simeq Gm_e/(h_e l_e)$ and the other is the tidal acceleration $a_{t,e} = GM_h h_e / R_e^3$. With $a_e = a_{t,e} + a_{g,e}$, condition (10) reduces to

$$a_{t,e} + a_{g,e} < \frac{\rho_{g,e} v_e^2}{\rho_e h_e} \equiv a_{r,e}, \quad (11)$$

which uses $\rho_e \gg \rho_{g,e}$. The relative velocity is computed by $v_{rel,e} = v_e \cos \theta_e \simeq v_e$ where $v_e = |\mathbf{v}_e|$ being the velocity of the element. This uses the approximation $\theta_e \ll 1$, which is satisfied along an element orbit, as soon as it leaves its apocentre. In addition, this value of $v_{rel,e}$ assumes that the background gas is at rest. The possibility of a lower relative velocity caused by radially falling background gas has been explored and leads to no significant difference. The right-hand side of equation (11) is called $a_{r,e}$ as it is equivalent to a ram pressure acceleration.

If condition (11) is satisfied, K-H instability then grows on a timescale

$$\tau_{KH,e} = \frac{1}{k_e v_{rel,e}} \frac{\rho_e + \rho_{g,e}}{\sqrt{\rho_{g,e} \rho_e}} \simeq \left(\frac{\rho_e}{\rho_{g,e}} \right)^{1/2} \frac{h_e}{v_e}, \quad (12)$$

for a given element³. Otherwise, the instability does not develop and $\tau_{KH,e} = +\infty$. K-H instability has time to fully grow before the element reaches pericentre if

$$f_{KH,e} \equiv \int_{T_e/2}^{T_e} \frac{dt}{\tau_{KH,e}} > 1, \quad (13)$$

where $T_e/2$ and T_e are the times corresponding to the element apocentre and pericentre passages respectively. Condition (13) can be understood by omitting the temporal dependence of $\tau_{KH,e}$. In this case, it reduces to $\tau_{KH,e} < T_e/2$ which clearly implies that the K-H instability has time to fully grow during the portion of orbit considered.

As an example, the evolution of $a_{g,e}$ (dotted lines), $a_{t,e}$ (dashed dotted lines), the right-hand side of equation (11) $a_{g,e} + a_{t,e}$ (solid line) and its right-hand side $a_{r,e}$ (dashed lines) is shown in Fig. 3 for three different elements of a stream produced by the disruption of the star in the red giant phase (profile RG1) by a black hole of mass $M_h = 10^8 M_\odot$ in a galaxy with $\eta = 10$. These elements have periods $T_e = 40$ yr (blue lines), $T_e = 160$ yr (red lines) and $T_e = 850$ yr (yellow lines). For all elements, tidal acceleration dominates self-gravity acceleration ($a_{t,e} > a_{g,e}$) in the final part of their orbit, when $R_e < h_e (M_h/m_e)^{1/3}$. The zones where condition (11) is true, are indicated by filled regions for each element. They only exist for the most bound (blue lines) and least bound (yellow lines) of the elements

³ In fact, $\tau_{KH,e} = (h_e / (a_{r,e} - a_{t,e} - a_{g,e}))^{1/2}$ and equation (12) assumes $a_{r,e} \gg a_{t,e} + a_{g,e}$. However, this approximation does not change our results.

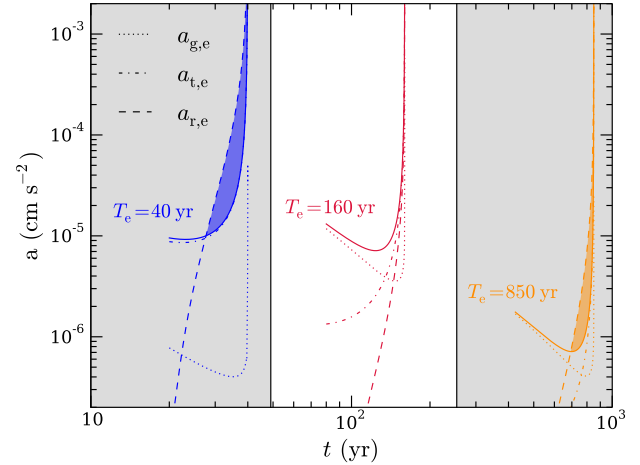


Figure 3. Evolution of $a_{g,e}$ (dotted lines), $a_{t,e}$ (dashed dotted lines), $a_{g,e} + a_{t,e}$ (solid line) and $a_{r,e}$ (dashed lines) for three elements of a stream produced by the tidal disruption of the star in the red giant phase (profile RG1) by a black hole of mass $M_h = 10^8 M_\odot$ in a galaxy with $\eta = 10$. The elements have different periods $T_e = 40$ yr (blue lines), $T_e = 160$ yr (red lines) and $T_e = 850$ yr (yellow lines). For each element, the filled areas indicate the regions where $a_{g,e} + a_{t,e} < a_{r,e}$, that is where condition (11) is satisfied. The grey areas indicate the range of periods of elements verifying condition (13), for which K-H instability has time to fully develop before they return to pericentre.

considered. For these two elements, condition (13) is also satisfied and K-H instability therefore has time to fully develop before they return to pericentre. For the intermediate element (red lines), condition (11) is never verified. This implies $f_{KH,e} = 0$ and condition (13) is therefore not satisfied either. The grey areas indicate the range of periods of all the stream elements that satisfy condition (13). On these elements, we expect K-H instability to fully grow over the course of their orbit.

Fig. 3 indicates the range of periods of elements that satisfy condition (13), but not the precise evolution of $f_{KH,e}$ with T_e . Actually, the transition between $f_{KH,e} = 0$ and $f_{KH,e} > 1$ is very sharp. For elements that never satisfy condition (11), $f_{KH,e} = 0$. However, as soon as condition (11) is met at some point along an element orbit, $f_{KH,e} \gtrsim 1$, which implies that condition (13) is already marginally satisfied. This is because, in the final part of an element orbit where $a_{t,e} \gg a_{g,e}$, condition (11) translates to $\tau_{KH,e} < (GM_h/R_e^3)^{-1/2}$, where the right-hand side is the infall time from R_e to pericentre. Omitting the time dependence of $\tau_{KH,e}$, this implies $f_{KH,e} > 1$.

The reason why only the most and least bound part of the stream are affected by K-H instability can be understood by examining condition (11) more in detail in the final part of each element orbit, where $a_{t,e} \gg a_{g,e}$. Using $v_e \simeq (GM_h/R_e)^{1/2}$, it reduces to

$$m_e/l_e < \rho_{g,e} R_e^2, \quad (14)$$

that is a condition on the stream linear density. Note that this condition is also independent on the element width h_e . Our results are therefore largely independent on the assumption of hydrostatic equilibrium made to compute this width in Section 3. One can clearly see that condition (14),

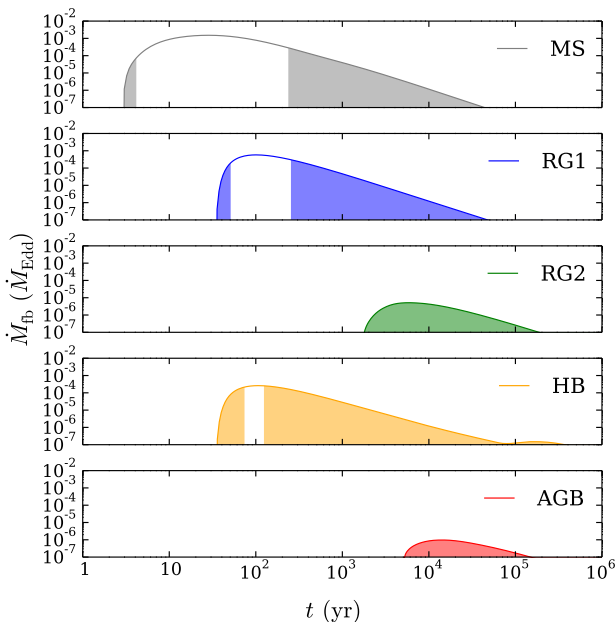


Figure 4. Evolution of the debris mass fallback rate after a disruption with $M_h = 10^8 M_\odot$ and $\eta = 10$ for the five stellar density profiles considered: MS (grey line), RG1 (blue line), RG2 (green line), HB (yellow line) and AGB (red line). The filled areas correspond to the return times of debris satisfying condition (13).

and therefore condition (13), is easily satisfied for the most bound part of the stream, which is less massive since it originates from the tenuous outer layer of the star. Although the least bound part of the stream contains more mass, it is stretched owing to different trajectories of neighbouring debris and condition (14) is also satisfied.

At this point, one can predict how the impact of K-H instability depends on the other parameters, namely the black hole mass M_h , the evolutionary stage of the star and η , which relates to the ambient medium density via equation (4). Tidal disruptions by more massive black holes lead to more extended streams. Furthermore, the right-hand side of condition (14) evaluated at R_t scales as $\rho_{g,e} R_e^2 \simeq \rho_g(R_t) R_t^2 \propto M_h^{9/15}$, which increases with the black hole mass. We therefore anticipate condition (11) to be more easily satisfied when M_h is larger. The stream is therefore likely to be more sensitive to K-H instability. This trend is also expected for disruptions of evolved stars as they also lead to more extended streams whose debris originate from a more tenuous outer layer. Finally, we anticipate the same tendency when η is increased, that is for environments with higher gas density, since $\rho_{g,e} R_e^2 \propto \eta$. These predictions will be verified explicitly in Section 4.3.

4.2 Ram pressure

As a stream element sweeps up the ambient medium located on its trajectory, it loses momentum and decelerates. This deceleration affects significantly the trajectory of the element once it has swept a mass of ambient gas larger than its own mass. This is equivalent to

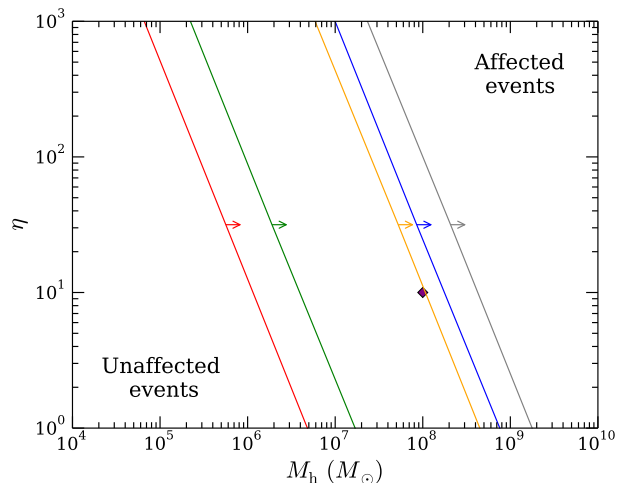


Figure 5. $M_h - \eta$ plane depicting the effect of K-H instability on different disruption events. Each line corresponds to one of the stellar density profiles considered. The zone in the direction of the arrow corresponds to events affected by K-H instability, for which $f_{KH,peak} > 1$. The zone in the opposite direction corresponds to events for which $f_{KH,peak} < 1$, unaffected by K-H instability. The purple diamond shows the parameters corresponding to Fig. 4, $M_h = 10^8 M_\odot$ and $\eta = 10$.

$$f_{ram,e} \equiv \frac{1}{m_e} \int_0^{T_e} \rho_e v_e A_e dt > 1, \quad (15)$$

where $A_e = h_e l_e \sin \theta_e$ is the element area sweeping gas from the ambient medium. As for K-H instability, we find this condition to be satisfied both for the most and least bound part of the stream. However, $f_{ram,e} < f_{KH,e}$ in all cases explored, which means that the debris are affected by K-H instability before their trajectories change due to ram pressure.

4.3 Effect on flare luminosities

We now evaluate the impact of K-H instability on the flare luminosities produced by the disruption of the star in different evolutionary stages and examine the dependence on the black hole mass M_h and ambient gas density, through the parameter η .

Fig. 4 shows the fallback rate, computed using equation (8), of the debris produced by the disruption of the star by a black hole of mass $M_h = 10^8 M_\odot$ in a galaxy with $\eta = 10$ for the five stellar density profiles considered. The filled areas indicate the times at which elements satisfying condition (13) return to pericentre. For these elements, K-H instability has time to fully grow over the course of their orbit. For profiles MS, RG1 and HB, these zones exist only for the most and least bound debris, as in the example of Fig. 3. The debris whose return times correspond to the peak fallback rate are always outside this zone. Instead, for profiles RG2 and AGB, all the elements lie in the filled zone, even those returning to pericentre when the fallback rate peaks. It means that K-H instability has time to fully grow in the whole stream. This confirms our expectation that streams produced by the disruption of evolved stars are more sensitive to K-H instability.

So far, we have examined for which elements condition (13) is satisfied, that is for which debris K-H instability fully

develop before they reach pericentre. As these instabilities involve the whole width of the stream, we infer that these debris subsequently dissolve into the ambient medium and do not return to pericentre.

Only the elements reaching pericentre intact can participate to the luminosity emitted from the event. Therefore, if all the stream dissolves into the ambient medium due to K-H instability, the appearance of the event is likely to be affected, emitting a significantly lower luminosity. We take a conservative approach and state that an event is affected by this instability if even the element corresponding to the peak of the mass fallback rate dissolves into the background gas. According to our criterion, this requires condition (13) to be satisfied for this element, that is $f_{\text{KH,peak}} > 1$. Fig. 5 shows the regions of the $M_{\text{h}} - \eta$ corresponding to events affected by K-H instability. Each line is associated to one of the stellar density profiles considered. The zone in the direction of the arrow corresponds to affected events while the zone in the opposite direction corresponds to unaffected events. The example discussed above ($M_{\text{h}} = 10^8 M_{\odot}$ and $\eta = 10$) where only the AGB and RG2 star events are affected is indicated by a purple diamond. As predicted above, events involving more massive black holes or occurring in galactic nuclei with denser gaseous environment are more sensitive to K-H instability.

5 IMPACT ON THE DETECTABILITY OF TDES

In the previous section, we argued that K-H instability can lead to the dissolution of a significant part of the stream before it comes back to pericentre, which could significantly reduce the luminosity emitted from the associated event. Furthermore, we showed that events involving more massive black holes and/or evolved stars are more sensitive to this effect. In this section, we examine the consequence on the detectability of TDEs produced by the disruption of a $1.4 M_{\odot}$ star in different evolutionary stages and by black hole of different masses.

For an event to lead to a substantial flare, the star must be disrupted outside the black hole's Schwarzschild radius R_{s} . Otherwise, it is swallowed whole without significant emission. We investigate the effect of K-H instability on the detectability of events satisfying this condition. To this aim, we define the probability of such events to occur when the star is in a given evolutionary stage by

$$f_{\text{flaring}}^{\text{stage}} = N_{\text{stage}}/N_{\text{lifetime}}, \quad (16)$$

where N_{stage} and N_{lifetime} are the number of events occurring during the evolutionary stage and the whole stellar lifetime respectively. The possibility of an event to be affected by K-H instability is only included in N_{stage} . These numbers are obtained by

$$N_{\text{stage}} = \int_{t_{\text{start}}}^{t_{\text{end}}} \dot{N} \chi_{\text{swa}} \chi_{\text{KH}} dt, \quad (17)$$

$$N_{\text{lifetime}} = \int_0^{t_{\text{lt}}} \dot{N} \chi_{\text{swa}} dt, \quad (18)$$

where t_{start} and t_{end} are the starting and ending times of the stage respectively, while t_{lt} is the lifetime of the star. In

equation (17), \dot{N} is the disruption rate, which we assumed to scale as $\dot{N} \propto R_{\text{t}}^{1/4}$ following MacLeod et al. (2012). χ_{swa} and χ_{KH} are binary functions given by

$$\chi_{\text{swa}} = \begin{cases} 0 & \text{if } R_{\text{t}} \leq R_{\text{s}} \\ 1 & \text{otherwise} \end{cases}, \quad (19)$$

$$\chi_{\text{KH}} = \begin{cases} 0 & \text{if } f_{\text{KH,peak}} \geq 1 \\ 1 & \text{otherwise} \end{cases}, \quad (20)$$

which are respectively zero if the star is swallowed whole and if the stream is affected by K-H instability according to the criterion defined in Section 4.

This probability is shown in Fig. 6 as a function of the black hole mass for different evolutionary stages. The left panel does not take into account K-H instability, artificially fixing $\chi_{\text{KH}} = 1$ in equation (17). It reproduces figure 14 (right panel) of MacLeod et al. (2012). For $M_{\text{h}} \gtrsim 10^8 M_{\odot}$, the black hole diet changes from mainly main sequence stars to giant stars. This is because $R_{\text{t}} < R_{\text{s}}$ for main sequence stars above this mass. Instead, the right panel of Fig. 6 includes the effect of K-H instability. The grey zone indicates affected events in a galaxy with $\eta = 10$. As previously, the black hole diet changes from main sequence stars to giants at $M_{\text{h}} \gtrsim 10^8 M_{\odot}$. However, as giant stars are more sensitive to K-H instability, all the events are affected by K-H instability for $M_{\text{h}} \gtrsim 10^9 M_{\odot}$, which could significantly hamper their detection. The blue lines indicates boundary of the grey areas for different values of η : 1,100,1000 from right to left. For $\eta > 100$, even the events involving main sequence stars are affected by K-H instability.

6 DISCUSSION AND CONCLUSION

The interaction between the debris stream produced by TDEs and the background gas of quiescent galaxies has often been neglected, on the basis of their large difference in density. In this paper, we have investigated this interaction for the bound part of the stream, involved in the flaring activity of these events. Through an analytical argument, we have demonstrated that K-H instability can affect the debris, especially for disruptions involving an evolved star and/or a massive black hole. In this case, a substantial fraction of the tidal stream can dissolve into the background gas before it reaching pericentre, likely leading to a flare dimmer than previously expected.

In order to model the stream, we have used the analytical model of Lodato et al. (2009) for the specific energy distribution within the stream, which assumes that the star is unperturbed until it reaches pericentre. Actually, numerical simulations have shown that the stellar structure is perturbed at pericentre (Lodato et al. 2009; Guillochon & Ramirez-Ruiz 2013). However, this effect can be easily accounted for within the same analytical model, by applying a homologous expansion of the unperturbed model by a factor ~ 2 (Lodato et al. 2009), which makes the energy distribution very close to the one obtained through simulations. This leads to a stream slightly more resistant to K-H instability but does not affect our main conclusions.

Another assumption of the model is a total disruption of the star by the black hole. However, simulations have shown that a surviving core can remain after the disruption (Guillochon & Ramirez-Ruiz 2013), which keeps following

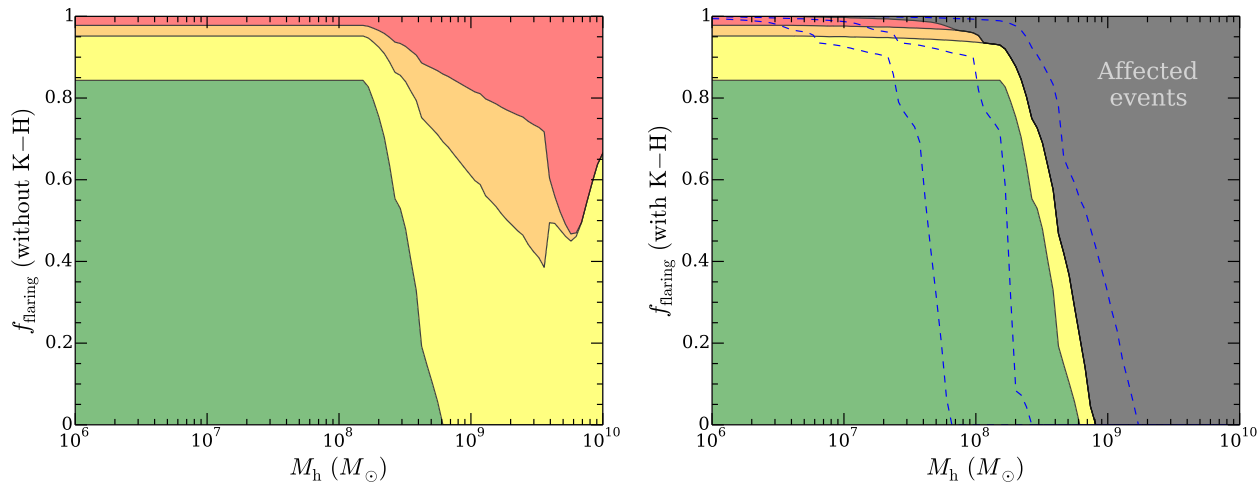


Figure 6. Probability for a disruption event to occur in a given evolutionary stage as a function of M_h . The different coloured areas correspond to different phases in the evolution of the star: main sequence (green), red giant (yellow), horizontal branch (orange) and asymptotic giant branch (red). Only the right panel includes the effect of K-H instability, with the grey zone corresponding to affected events for a galaxy with $\eta = 10$. The boundary of this zone is shown by blue dashed lines for other values of η : 1, 100 and 1000 from right to left.

the initial stellar orbit. This likely causes the marginally bound part of the stream to contain less mass than expected from Lodato et al. (2009). The debris returning to pericentre at late times would therefore be even more sensitive to K-H instability.

In addition, any magnetic field has been neglected in the stream. However, it could prevent the dissolution of the stream by K-H instability (McCourt et al. 2015)

Finally, our calculations are made in an ambient medium at rest although an inward velocity of the gas environment could diminish the effect of K-H instability. We have tested the dependence of our results on this assumption by introducing a radial velocity of the gas, which results in a lower relative velocity in equations (11) and (12). We find that our main conclusions remain unchanged for an infall velocity up to the Keplerian velocity, thus confirming the solidity of our analysis.

The main implication of this study is that any TDEs involving black holes with masses $\gtrsim 10^8 M_\odot$ might be difficult to detect, a conclusion largely independent of our scaling for the background gas density with black hole mass. This was already known for main sequence stars, which are swallowed whole for this range of masses (MacLeod et al. 2012). Here, we show that this is also the case for giant stars, which have their debris stream dissolved into the background gas through K-H instability.

REFERENCES

Alexander K. D., Berger E., Guillochon J., Zauderer B. A., Williams P. K. G., 2015, ArXiv e-prints
 Berger E., Zauderer A., Pooley G. G., Soderberg A. M., Sari R., Brunthaler A., Bietenholz M. F., 2012, ApJ, 748, 36
 Bonnerot C., Rossi E. M., Lodato G., Price D. J., 2015, ArXiv e-prints

Clarke C., Carswell B., 2007, Principles of Astrophysical Fluid Dynamics
 Coughlin E. R., Nixon C., 2015, ApJL, 808, L11
 Coughlin E. R., Nixon C., Begelman M. C., Armitage P. J., Price D. J., 2015, ArXiv e-prints
 Cuadra J., Nayakshin S., Springel V., Di Matteo T., 2006, MNRAS, 366, 358
 Frank J., Rees M. J., 1976, MNRAS, 176, 633
 Gebhardt K. et al., 2000, ApJL, 539, L13
 Genozov A., Stone N. C., Metzger B. D., 2015, MNRAS, 453, 775
 Gezari S. et al., 2012, Nat, 485, 217
 Guillochon J., Manukian H., Ramirez-Ruiz E., 2014, ApJ, 783, 23
 Guillochon J., McCourt M., Chen X., Johnson M. D., Berger E., 2015, ArXiv e-prints
 Guillochon J., Ramirez-Ruiz E., 2013, ApJ, 767, 25
 Hayasaki K., Stone N., Loeb A., 2013, MNRAS, 434, 909
 Hayasaki K., Stone N. C., Loeb A., 2015, ArXiv e-prints
 Kelley L. Z., Tchekhovskoy A., Narayan R., 2014, MNRAS, 445, 3919
 Kochanek C. S., 1994, ApJ, 436, 56
 Komossa S., 2015, Journal of High Energy Astrophysics, 7, 148
 Komossa S., Halpern J., Schartel N., Hasinger G., Santos-Lleo M., Predehl P., 2004, ApJL, 603, L17
 Lodato G., King A. R., Pringle J. E., 2009, MNRAS, 392, 332
 MacLeod M., Guillochon J., Ramirez-Ruiz E., 2012, ApJ, 757, 134
 McConnell N. J., Ma C.-P., Gebhardt K., Wright S. A., Murphy J. D., Lauer T. R., Graham J. R., Richstone D. O., 2011, Nat, 480, 215
 McCourt M., O’Leary R. M., Madigan A.-M., Quataert E., 2015, MNRAS, 449, 2
 Paxton B., Bildsten L., Dotter A., Herwig F., Lesaffre P., Timmes F., 2011, ApJS, 192, 3
 Quataert E., 2004, ApJ, 613, 322

- Ramirez-Ruiz E., Rosswog S., 2009, *ApJL*, 697, L77
Rees M. J., 1988, *Nat*, 333, 523
Rimoldi A., Rossi E. M., Piran T., Portegies Zwart S., 2015,
MNRAS, 447, 3096
Shiokawa H., Krolik J. H., Cheng R. M., Piran T., Noble
S. C., 2015, *ArXiv e-prints*
Wang Q. D. et al., 2013, *Science*, 341, 981